Editors' Suggestion

Comparing magnetic ground-state properties of the V- and Cr-doped topological insulator $(Bi, Sb)_2Te_3$

A. Tcakaev,[1] V. B. Zabolotnyy,[1,*] R. J. Green,[2,3] T. R. F. Peixoto,[4] F. Stier,[1] M. Dettbarn,[1] S. Schreyeck,[5] M. Winnerlein,[5] R. Crespo Vidal,[4] S. Schatz,[4] H. B. Vasili,[6] M. Valvidares,[6] K. Brunner,[5] C. Gould,[5] H. Bentmann,[4] F. Reinert,[4] L. W. Molenkamp,[5] and V. Hinkov[1,†]

[1]*Experimentelle Physik IV and Röntgen Research Center for Complex Materials (RCCM), Fakultät für Physik und Astronomie, Universität Würzburg, Am Hubland, D-97074 Würzburg, Germany*

[2]*Department of Physics and Astronomy and Stewart Blusson Quantum Matter Institute, University of British Columbia, Vancouver, British Columbia, Canada V6T 1Z4*

[3]*Department of Physics and Engineering Physics, University of Saskatchewan, Saskatchewan, Saskatoon, Canada S7N 5E2*

[4]*Experimentelle Physik VII and Röntgen Research Center for Complex Materials (RCCM), Fakultät für Physik und Astronomie, Universität Würzburg, Am Hubland, D-97074 Würzburg, Germany*

[5]*Institute for Topological Insulators and Physikalisches Institut, Experimentelle Physik III, Universität Würzburg, Am Hubland, D-97074 Würzburg, Germany*

[6]*ALBA Synchrotron Light Source, E-08290 Cerdanyola del Vallès, Barcelona, Spain*

(Received 8 August 2019; revised manuscript received 8 January 2020; published 27 January 2020)

An insulating ferromagnetic ground state is a fundamental prerequisite for the quantum anomalous Hall (QAH) effect observed in magnetically doped topological insulators such as $(Bi, Sb)_2Te_3$. So far, the QAH effect could only be induced by V and Cr doping, with V resulting in ferromagnetism with a higher T_C and a more robust QAH state. To better understand the difference between the two dopants, we have investigated epitaxial $V_{0.1}Sb_{1.9}Te_3$ and $Cr_{0.1}(Bi_{0.1}Sb_{0.9})_{1.9}Te_3$ films using x-ray absorption spectroscopy and x-ray magnetic circular dichroism. Our analysis of the V and Cr $L_{2,3}$ spectra by multiplet ligand-field theory goes beyond existing studies by allowing several charge-transfer states. We find a strongly covalent ground state, dominated by the superposition of one and two Te-ligand-hole configurations, with a negligible contribution from ionic V^{3+} or Cr^{3+}. Crucial for a comparison with theoretical models are the resulting d-shell fillings ($n_d^{V} = 3.47$ and $n_d^{Cr} = 4.33$), and spin ($m_{spin}^{V} = 2.39\mu_B$ and $m_{spin}^{Cr} = 3.22\mu_B$) and orbital ($m_{orb}^{V} = -0.55\mu_B$ and $m_{orb}^{Cr} = -0.03\mu_B$) magnetic moments, with the total magnetic moments being in good agreement with published magnetometry results. Our findings indicate the importance of the Te $5p$ states for the ferromagnetism in $(Bi, Sb)_2Te_3$ and favor theories involving pd-exchange.

DOI: 10.1103/PhysRevB.101.045127

I. INTRODUCTION

Tetradymite chalcogenides such as Bi_2Se_3, Bi_2Te_3, and Sb_2Te_3 are narrow-band semiconductors, which were among the first compounds shown to exhibit symmetry-protected topological surface states [1,2], briefly after the realization of the two-dimensional analog in HgTe quantum wells [3]. This nontrivial topology, along with an insulating ferromagnetic (FM) state [2,4], are the two most fundamental prerequisites for the realization of the quantum anomalous Hall (QAH) effect. Ferromagnetism can be achieved by doping with various transition metal atoms (TM), such as V, Cr, Mn, or Fe [5–10]. However, to date, the QAH effect has been only observed in V- and Cr-doped $(Bi, Sb)_2Te_3$ systems [11–14], with V doping providing a more robust FM order and higher T_C, which is in turn favorable for realizing the QAH effect at higher temperatures [15]. Since the nature of FM coupling is not yet well understood [13], establishing microscopic differences between the strongly correlated V and Cr impurities would help with evaluating the relevance of the various proposed models of FM coupling [4,16–19] and eventually provide better control of the QAH effect [12,15].

The requirement of an insulating FM state rules out coupling mechanisms based on free carriers such as in diluted magnetic semiconductor (DMS) scenarios [20,21]. Hence, it was hypothesized that a sizable Van Vleck spin susceptibility may be responsible for the FM coupling between the dopants [4]. Early electron energy loss spectroscopy data were interpreted as being in support of this mechanism [22].

However, recent studies using resonant photoemission spectroscopy (resPES) [23] and x-ray magnetic circular dichroism (XMCD) [24], as well as *ab initio* calculations [16,19], indicate that the Van Vleck mechanism is insufficient to explain the complex ferromagnetic state in V- and Cr-doped $(Bi, Sb)_2Te_3$. Moreover, alternative mechanisms based on the Zener-type pd-exchange interaction were brought into focus, including double and superexchange [23–25]. In this context,

*Corresponding author: volodymyr.zabolotnyy@physik.uni-wuerzburg.de

†Corresponding author: hinkov@physik.uni-wuerzburg.de

spin-polarized first-principles calculations predict a reduced exchange interaction with increasing d-shell electron occupation n_d [25], which seems to agree with the observation of a more robust FM order with a higher T_C in the case of V doping as compared to Cr [12]. Comparative theoretical studies of different dopants show that the exact configuration of the TM impurity [26,27] is essential for the magnetic coupling and requires its experimental determination.

Often, n_d is inferred from the nominal valence of the dopant in a simplified ionic picture [7,12,28]. But even in comparatively more ionic oxides this picture is of limited use since the effects of charge transfer—and the electronic correlations in the d shell—cannot be neglected [29,30]. Earlier x-ray absorption spectroscopy (XAS) and XMCD studies already indicated the covalent character of Cr doping in $(Bi, Sb)_2(Se, Te)_3$ [31,32], yet within a pared down atomic multiplet model considering only one ligand hole.

Despite the fact that vanadium, rather than chromium, doping is the more promising avenue to optimized QAH properties [12], only qualitative XAS and XMCD studies of $V_z(Bi, Sb)_{2-z}Te_3$ have been published so far [24,33–36]. In the present paper, we provide a comprehensive XAS and XMCD comparison of V- and Cr-doped $(Bi, Sb)_2Te_3$ thin films, grown on Si(111) using molecular beam epitaxy (MBE). We model the detailed line shapes of the V and Cr spectra collected from freshly prepared surfaces with multiplet ligand-field theory (MLFT) calculations and determine their correlated many-particle ground states. Our analysis allows us to bypass XMCD sum rules and directly determine the values of both the orbital and spin moments, which are in good agreement with published magnetometry results [12,34]. We find a strongly covalent ground state of the magnetic impurities dominated by the coherent superposition of one and two Te-ligand-hole configurations, with negligible contributions from a purely ionic 3+ configuration. The strong charge transfer from the ligands found in this work indicates the importance of Te $5p$ states for the magnetic coupling and, thus, the QAH effect in magnetically doped topological insulators (TIs).

II. EXPERIMENT

The samples investigated consist of about 9-nm-thick $Cr_z(Bi_{1-x}Sb_x)_{2-z}Te_3$ and $V_zSb_{2-z}Te_3$ films with $x = 0.9$ and $z = 0.1$, grown by MBE on H passivated Si(111) substrates. The detailed growth conditions can be found elsewhere [37,38]. After the growth of the films, a 100-nm Te cap layer was deposited *in situ*, in order to protect the surface from contamination during sample transport. The morphology, thickness, and crystallinity of the layers were characterized by atomic force microscopy (AFM) at ambient conditions, x-ray reflectivity (XRR) measurements, and x-ray diffraction (XRD).

The XAS and XMCD measurements at the V and Cr $L_{2,3}$ absorption edges were performed using the high-field cryomagnet end station HECTOR of the BOREAS beamline at the ALBA synchrotron radiation facility (Barcelona, Spain) [39]. The samples were glued with conducting silver paint onto Cu sample plates and mounted on the cold finger of a helium flow cryostat. Prior to the measurements, the Te capping layer

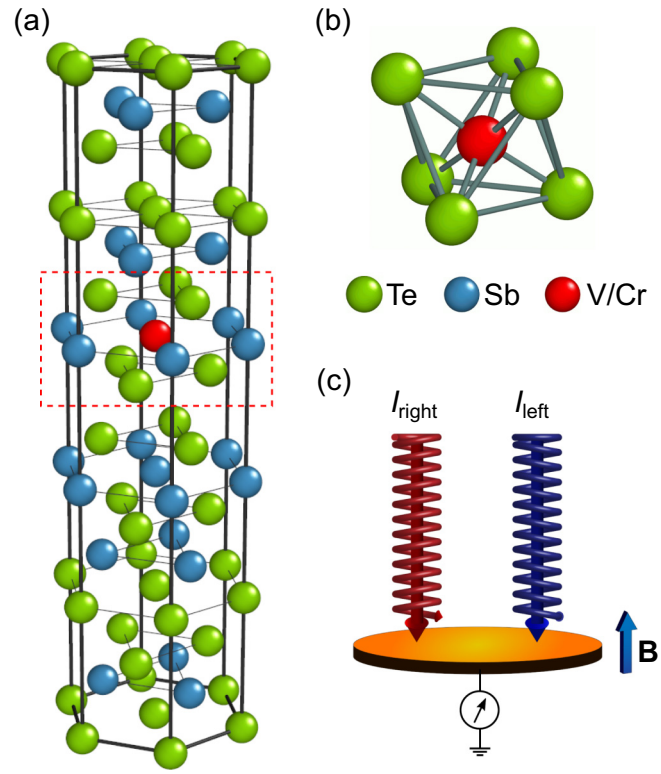

FIG. 1. (a) Crystal structure of V/Cr-doped Sb_2Te_3 consisting of stacked quintuple layers along the c axis (Te-Sb-Te-Sb-Te), separated by van der Waals gaps. (b) The V/Cr impurity substitutes Sb, which is surrounded by six Te atoms. The impurity atom has a slightly trigonally distorted O_h symmetry. The gray sticks are shown to highlight the octahedron and are not generally representative of chemical bonds. (c) Schematics of the experimental geometry for the XMCD measurements. The polarized and monochromatized photons are absorbed by the sample in a magnetic field applied parallel to the direction of the incoming beam. The x-ray absorption spectra are obtained by measuring the drain current (TEY).

was mechanically removed in the fast-entry chamber at a pressure of $\sim 10^{-9}$ mbar. The sample was then transferred into the spectroscopy chamber operated under UHV conditions, with a base pressure in the 10^{-11} mbar range. Previously, we had demonstrated the effectiveness of this method to expose a clean sample surface using Bi_2Te_3 [40]. We collected spectra encompassing the oxygen edge at the beginning and at the end of the measurements for each sample, which demonstrate that the surfaces have not changed throughout the experiment.

XAS measurements were carried out at 2 K by measuring the total electron yield (TEY) via the sample drain current normalized by the incoming photon intensity, giving a probing depth of 3–5 nm [41]. Circularly polarized x rays with close to 100% polarization were used in normal incidence with respect to the sample surface and parallel to the applied magnetic field, as schematically illustrated in Fig. 1(c). The area probed by the beam (about $100 \times 80\ \mu m^2$) is much smaller than the sample size. The raw XAS spectra I_{left} and I_{right} measured with the helicity vector antiparallel [left (L)] and parallel [right (R)] to the fixed magnetic field of 3 T were scaled with respect to each other to have the same intensity at energies

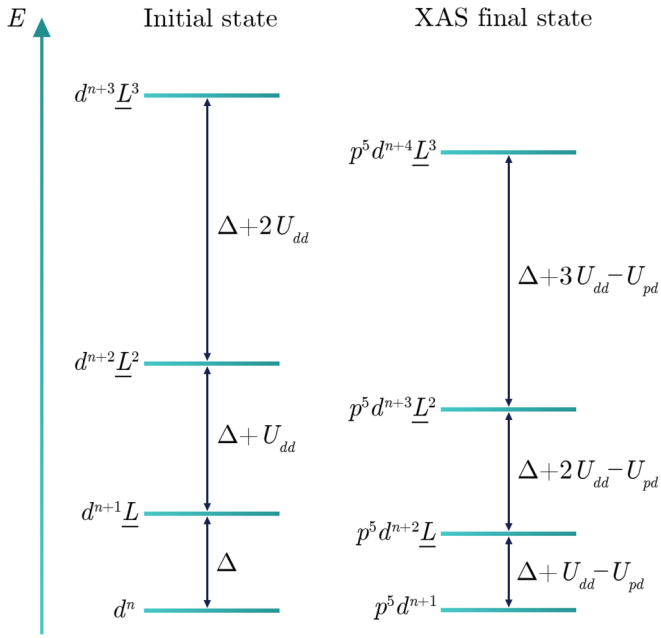

FIG. 2. Schematic diagram showing the on-site energies of the various configurations for the initial state and XAS final state when the hybridization (V_{e_g}) is zero.

far from the resonances. We define the average XAS as $I_{\text{avg}} = (I_{\text{left}} + I_{\text{right}})/2$. Since only the resonant part of the spectra enters the sum rules, we subtract the background including the continuum edge jumps from the raw spectra: $I^{\text{res}}_{\text{left/right}} = I_{\text{left/right}} - I_{\text{bg}}$. The normalized XMCD signal then becomes $I_{\text{XMCD}} = (I^{\text{res}}_{\text{left}} - I^{\text{res}}_{\text{right}})/(I^{\text{res}}_{\text{left}} + I^{\text{res}}_{\text{right}})$. To cancel out any experimental drifts, for each XMCD we actually measured eight spectra in a row by altering the polarization according to the pattern LRRL LRRL.

III. MULTIPLET LIGAND-FIELD THEORY CALCULATIONS

For the interpretation of $2p \rightarrow 3d$ x-ray absorption spectra, MLFT calculations are an essential tool, which allows the description of both ground-state properties and spectra of $3d$ elements. The reasons why these calculations, which are not *ab initio* and consider only the local symmetry of an ion, lead to such an excellent agreement with experiment [42–44] are that within the MLFT calculations the initial and final states are both taken into account and electron correlations, spin-orbit coupling, crystal field, and charge-transfer effects are included. This means that detailed information concerning the initial state can be obtained once the spectrum has been reproduced.

In this work, XAS and XMCD spectra for the V and Cr $L_{2,3}$ ($2p \rightarrow 3d$) absorption edges were calculated within the configuration-interaction scheme, considering a cluster consisting of the central transition metal cation surrounded by six tellurium ligands, as depicted in Figs. 1(a) and 1(b). We consider the nominal $2p^63d^2$ (V^{3+}) and $2p^63d^3$ (Cr^{3+}) configuration and further employ three additional charge-transfer states $d^{n+1}\underline{L}$, $d^{n+2}\underline{L}^2$, and $d^{n+3}\underline{L}^3$ to account for covalence effects (see Fig. 2). Here, $\underline{L}^p$ denotes p holes in the Te $5p$ orbitals. In this manner, we go beyond existing atomic multiplet theory calculations performed for Cr in Bi_2Se_3 [31,45] and in Sb_2Te_3 [32], where only states with one ligand hole $d^{n+1}\underline{L}$ were considered, as well as beyond crystal-field multiplet calculations for Cr in Bi_2Te_3 [46]. It has been demonstrated that for highly covalent compounds (as those investigated in this work) the reduced basis calculations, in which at most one hole is allowed at the ligand site, overestimate the ionic character [47]. This is further confirmed by the results of this work. With our basis set the ground state of the cluster can be written as

$$|\Psi_{\text{GS}}\rangle = |\Psi_n\rangle + |\Psi_{n+1}\rangle + \cdots + |\Psi_{n+p}\rangle\,, \tag{1}$$

where $|\Psi_{n+p}\rangle = c_p\,|d^{n+p}\underline{L}^p\rangle$ and $\langle\Psi_{n+p}|\Psi_{n+p}\rangle = c_p^2$ give the weight of each configuration. In the same manner, the XAS final state is described by a linear combination of p^5d^{n+1}, $p^5d^{n+2}\underline{L}$, $p^5d^{n+3}\underline{L}^2$, and $p^5d^{n+4}\underline{L}^3$. To fit the experimental XAS and XMCD spectra, we introduce the following fit parameters in the MLFT calculation: the scaling parameter β for the Hartree-Fock values of the Slater integrals; the charge-transfer (CT) energy $\Delta = E(d^{n+1}\underline{L}) - E(d^n)$ it costs to bring one electron from the ligand p to the TM d shell; the Coulomb interaction energies U_{dd} between the valence $3d$ electrons and U_{pd} between the $2p$ core electron and $3d$ electron; and covalent hopping integrals $V_{t_{2g}} = 2pd\pi$ and $V_{e_g} = -\sqrt{3}pd\sigma$ between the p orbitals at the ligand sites and the TM $3d$ orbitals of t_{2g} and e_g symmetry, respectively. Apart from the above terms, we also consider the crystal-field splitting parameter $10Dq$. We assume V or Cr to substitute Sb or Bi on the cation sites and describe the crystal field in octahedral (O_h) symmetry, with the C_4 axes of the octahedron along the TM-Te bonds [see Fig. 1(b)]. There is a slight distortion from a perfect octahedral (O_h) to trigonal (C_{3v}) symmetry. Within a point charge model, the distortion would result in an energy splitting of the t_{2g} orbitals of less than 2% as compared to $10Dq$. This is much smaller than the energy resolution of the XAS experiment and justifies our approximation.

Adopting published results [48–51], we fix U_{dd}/U_{pd} to 0.83 and $pd\sigma/pd\pi$ to −2.0, which also allows us to reduce the parameter space and speed up fitting. Spin-orbit coupling was kept at its Hartree-Fock value. The simulations were performed using the QUANTY software package for quantum many-body calculations, developed by Haverkort [52]. The spectral contributions from each of the split ground-state terms to the absorption spectra were weighted by a Boltzmann factor corresponding to the experimental temperature of $T \approx 2$ K. The mean-field effective potential was accounted for by introducing an exchange field term acting on the spin. We estimated the exchange field from the Curie temperature ($T_C = 45$ K for the V-doped sample and $T_C = 20$ K for the Cr-doped one, as shown in Fig. 4). Since the experiments were performed in an external magnetic field of 3 T, this was also included in the Hamiltonian. To account for the instrumental and intrinsic lifetime broadening, the calculated spectra were convoluted with a Gaussian function of 0.3 eV full width at half maximum (FWHM) and with an energy-dependent Lorentzian profile of 0.2–0.3 eV FWHM.

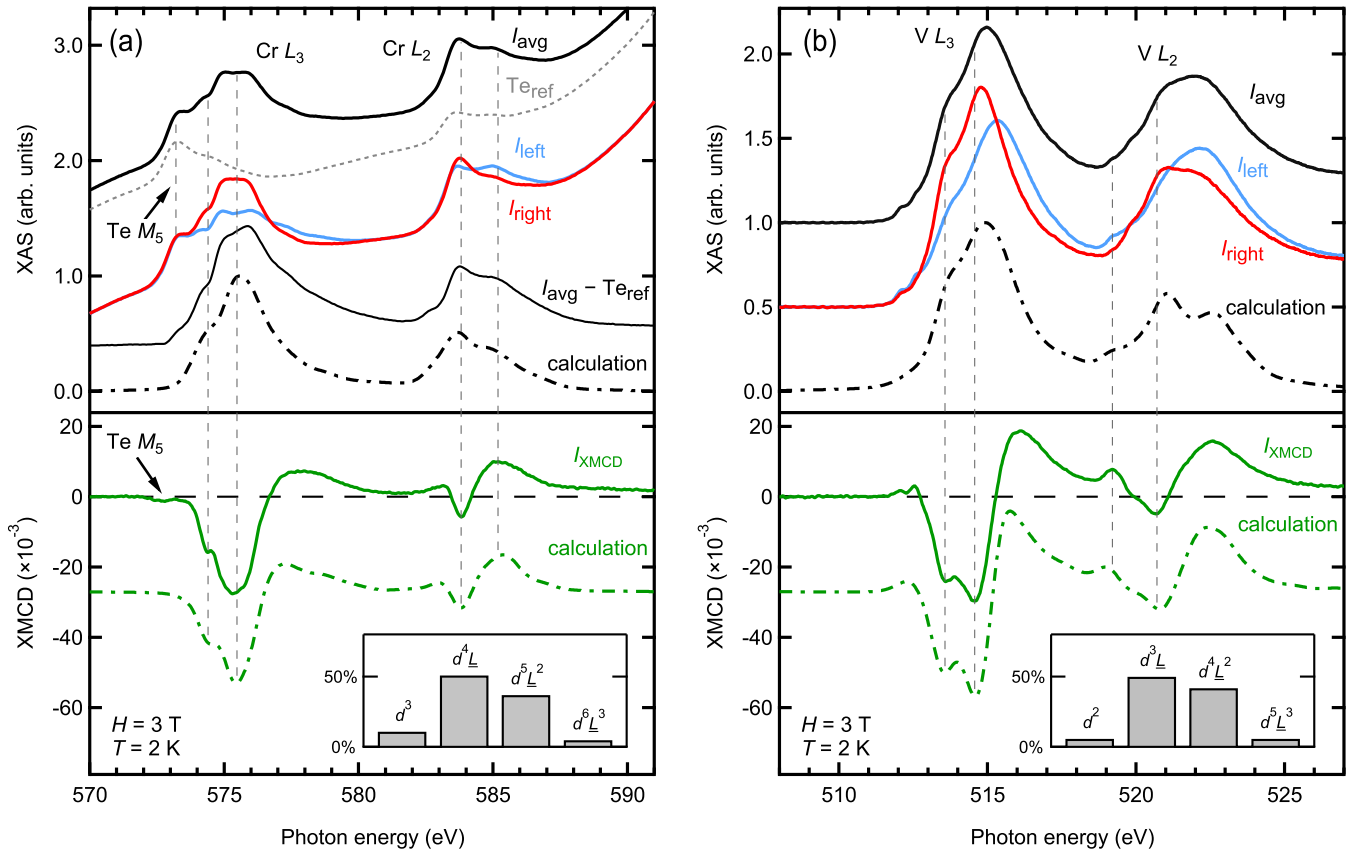

FIG. 3. Experimental and calculated $L_{2,3}$ XAS and XMCD spectra. (a) $Cr_{0.1}(Bi_{0.1}Sb_{0.9})_{1.9}Te_3$ film. (b) $V_{0.1}Sb_{1.9}Te_3$ film. The top panels show experimental x-ray absorption data, obtained as described in Sec. II (left-circular polarization I_{left}, light blue line; right-circular polarization I_{right}, dark red line; averaged over both polarizations I_{avg}, bold black line). Polarization-averaged spectra calculated by the MLFT cluster model described in the text are shown as a dashed-dotted line; to facilitate the comparison with experiment, in (a) we show Cr data (thin black line) corrected for the Te contribution using a Cr-free reference sample (Te_{ref}, dotted gray line). The bottom panels show the corresponding normalized experimental (I_{XMCD}, solid green line) and calculated XMCD spectra (dashed-dotted green line). The insets show the contributions of different configurations to the ground state. The dashed vertical lines are drawn as a guide to the eye, highlighting the position of particular features in the spectra. The peak intensity of the calculated XAS spectrum was normalized to one.

IV. RESULTS AND DISCUSSIONS

A. V and Cr $L_{2,3}$ XAS and XMCD

In Fig. 3 we compare the measured and calculated $L_{2,3}$ edge XAS and XMCD spectra for both the Cr- and V-doped samples. The Cr $L_{2,3}$ edges largely overlap with Te $M_{4,5}$ spectral features, which complicates the detailed comparison of experimental x-ray absorption spectra with calculations. To demonstrate this, we have highlighted the Te M_5 peak in Fig. 3(a). The overlap with the Te $M_{4,5}$ features, which extend to higher energies beyond the shown energy range, is the main reason for the strongly sloping background in the measured XAS. To simplify the visual comparison we have subtracted the Te $M_{4,5}$ spectrum measured in a Cr-free reference sample [Fig. 3(a), gray dotted line]. With the Te contribution eliminated, it is now obvious that at the main Cr L_3 peak the spectrum shows a double-peak structure. It should be noted that this double-peak feature is not due to the oxidation of Cr ions on the surface: Such oxidized surface Cr was reported for the Cr:Bi_2Se_3 system, its main contribution to both XAS and XMCD being ~1.5 eV higher in energy [45]. Here, we see no sign of oxidized surface Cr, which testifies to the purity of the sample surface. There is no indication of oxidized vanadium in the XAS data of the V-doped sample, either. It is noteworthy that the vanadium spectrum reveals a significant shoulder structure at the low-energy flank of the L_3 main peak. Overall, despite the high experimental resolution, both the Cr and V spectral line shapes are rather broad, showing no sharp multiplet structure, which is an indication of the strong covalence of the systems [41].

The corresponding normalized XMCD spectra at the V/Cr $L_{2,3}$ edges, displayed in the bottom panels of Fig. 3, exhibit a persistent ferromagnetic state at low temperatures and a sizable magnetic moment carried by the TM 3d states. In Fig. 4 we show the strength of the XMCD signal as a function of temperature measured in the remanent state (10 mT). The thermal demagnetization curves indicate that the V-doped sample exhibits more robust ferromagnetism, with the Curie temperature ($T_C \sim 45$ K) more than twice as high as that of the Cr-doped sample ($T_C \sim 20$ K), in good agreement with previous works [12,53]. The higher T_C is favorable to achieve a stable QAH state at higher temperatures [12,15].

The most noteworthy feature in the XMCD line shape of both ions, shown in Fig. 3, is the peak on the low-energy side

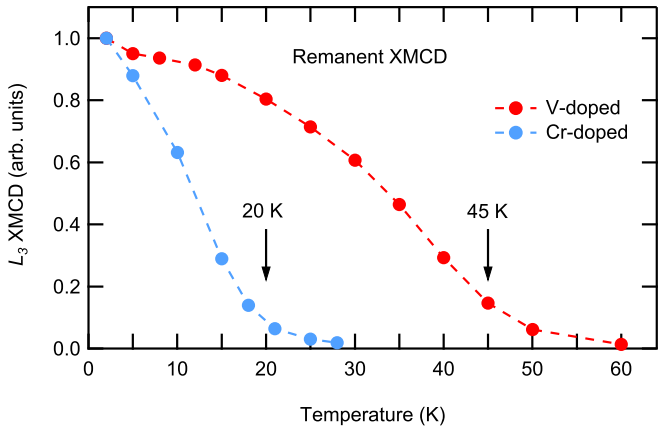

FIG. 4. Temperature dependence of the remanent (10 mT) XMCD signal at the V (red circles) and Cr (blue circles) L_3 edges, from which the corresponding Curie temperatures can be estimates as $T_C^{\mathrm{V}} \sim 45$ K and $T_C^{\mathrm{Cr}} \sim 20$ K. The XMCD signal at $T = 2$ K has been normalized to 1.0.

of the L_3 edge, which resembles the one observed in Cr_2Te_3 [54], a compound characterized by strong hybridization of the TM $3d$ band with the ligand $5p$ band. Moreover, it is notable that the dichroism at both the L_2 and the L_3 edge of V is more pronounced as compared to Cr. In general, the line shape of the XMCD spectrum depends on the spin polarization of the d band, defined as an imbalance between the number of spin-up and spin-down d holes. The XMCD signal shows a more asymmetric line shape of the $L_{2,3}$ edges for small spin polarizations (and hence small spin magnetic moments), and a more symmetric line shape for high spin polarizations [29].

Overall, our XAS and XMCD data are consistent with previous reports on (V, Cr):$(Bi, Sb)_2Te_3$ [12,23] thin films, as well as bulk samples [24,33,35,53].

B. Sum-rule results

In the following we report the results of a sum-rule analysis we applied to our data. Following the literature [55], we define the integrated dichroic spectral weight of the L_3 peak

$$p = \int_{E_0}^{E_{\mathrm{cutoff}}} \left[I_{\mathrm{left}}^{\mathrm{res}}(E) - I_{\mathrm{right}}^{\mathrm{res}}(E)\right] dE, \tag{2}$$

the total integrated dichroic spectral weight

$$q = \int_{E_0}^{E_1} \left[I_{\mathrm{left}}^{\mathrm{res}}(E) - I_{\mathrm{right}}^{\mathrm{res}}(E)\right] dE, \tag{3}$$

and the total integrated XAS spectral weight

$$r = \int_{E_0}^{E_1} \left[I_{\mathrm{left}}^{\mathrm{res}}(E) + I_{\mathrm{right}}^{\mathrm{res}}(E)\right] dE, \tag{4}$$

where E_0 and E_1 denote the onset and the end energy of the entire $L_{2,3}$ edges, and E_{cutoff} denotes the energy separating the L_3 and L_2 contributions, as shown in Fig. 5(a). The sum rules relate these integrated XMCD and XAS spectral weights of a specific shell to the ground-state orbital and spin magnetic moments m_{orb} and m_{spin}, respectively [56,57],

$$m_{\mathrm{orb}} = -\frac{4}{3}\frac{q}{r} n_h, \tag{5}$$

$$m_{\mathrm{spin}} = -\frac{6p - 4q}{r} n_h C + 7\langle T_z \rangle. \tag{6}$$

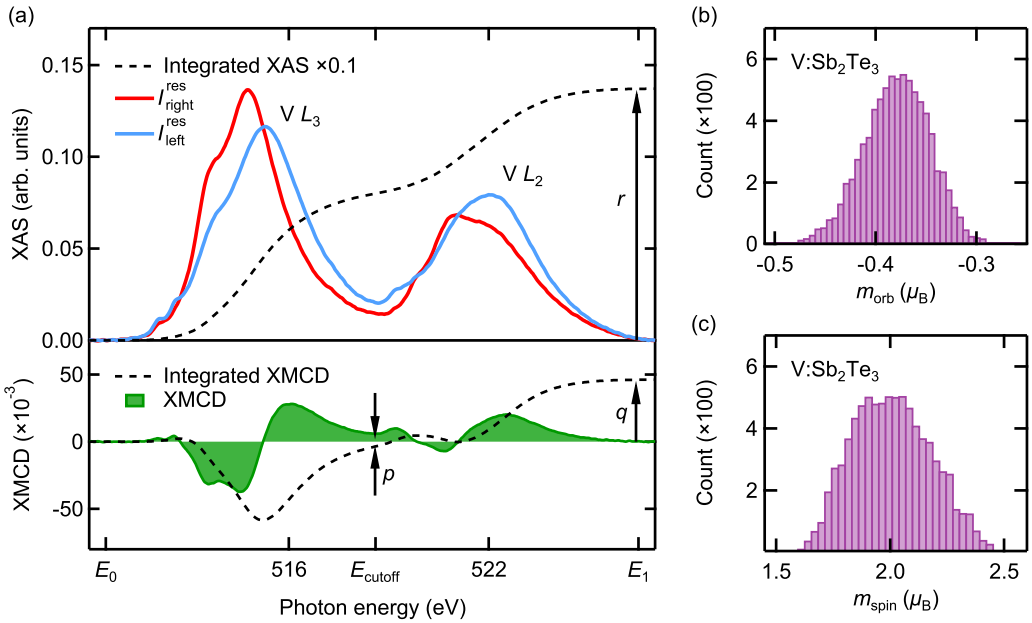

FIG. 5. Sum-rule analysis for the V-doped Sb_2Te_3 thin film. (a) Left- and right-circularly polarized XAS spectra of the V $L_{2,3}$ edges, obtained after the background correction described in Sec. II ($I_{\mathrm{left}}^{\mathrm{res}}$, solid, light blue line, and $I_{\mathrm{right}}^{\mathrm{res}}$, solid dark red line), along with the corresponding XMCD data (solid green line, lower panel). The dashed lines show the total integrated XAS and XMCD spectral weight, respectively. The arrows mark the values of r, p, and q used in Eqs. (5) and (6). (b) and (c) Distribution of m_{orb} and m_{spin}, respectively, obtained by applying the sum-rule analysis 8000 times, as described in the main text.

TABLE I. Optimized Hartree-Fock values of the Slater integrals and spin-orbit coupling constants for V^{3+} and Cr^{3+} ions (in units of eV).

Ion	State	Configuration	$F_{dd}^{(2)}$	$F_{dd}^{(4)}$	ζ_{3d}	$F_{pd}^{(2)}$	$G_{pd}^{(1)}$	$G_{pd}^{(3)}$	ζ_{2p}
V^{3+}	Initial	$2p^6\,3d^2$	6.583	4.130	0.027				
	Final	$2p^5\,3d^3$	7.133	4.477	0.036	3.937	2.853	1.622	4.650
Cr^{3+}	Initial	$2p^6\,3d^3$	7.544	4.728	0.035				
	Final	$2p^5\,3d^4$	8.117	5.089	0.047	4.568	3.350	1.905	5.668

Here, n_h stands for the number of $3d$ holes and $\langle T_z \rangle$ is the expectation value of the intra-atomic magnetic dipole operator. The magnetic dipole operator is given by [57,58]

$$\hat{\mathbf{T}} = \sum_i \hat{\mathbf{S}}_i - 3\hat{\mathbf{r}}_i(\hat{\mathbf{r}}_i \cdot \hat{\mathbf{S}}_i), \tag{7}$$

where the sum over i runs over all electrons. Knowing the ground state of the system from our multiplet calculations, we can readily estimate the expectation value of the magnetic dipole term: $\langle T_z \rangle = 0.08$ for V and $\langle T_z \rangle = 0.5 \times 10^{-3}$ for Cr. In Eqs. (5)–(7) all magnetic moments are measured in Bohr magnetons and the angular momenta in units of $\hbar$.

The applicability of the spin sum rule further depends on the question of how well the contributions of the L_3 ($j = 3/2$) and L_2 ($j = 1/2$) edges are separated in energy. Due to the strong jj mixing arising from the relatively small spin-orbit coupling in the $2p$ shell, there is a considerable overlap of these contributions for light TM elements such as V and Cr. Therefore, in our spectra the cutoff energy E_{cutoff} separating the $j = 3/2$ and $j = 1/2$ contributions is in principle ill defined. The correction factor C is introduced to compensate the resulting deviation. However, the determination of C obviously depends on the choice of E_{cutoff} and requires further modeling of the data, thus strongly limiting the usability of the spin sum rule for light TM elements. Here, we followed the approach of Refs. [59,60] to obtain C: We formally applied the spin sum rule to our cluster-model-based theoretical spectrum and derived $C = 1.7$ for Cr and $C = 1.2$ for V by comparison with the spin moment directly calculated for the ground state of the same model.

Since the extracted magnetic moments depend in a nontrivial way on the input parameters controlling the normalization and background subtraction procedures described in Sec. II, as well as on the integration energy and n_h, we vary the input parameters in a random and uncorrelated way within the assumed confidence intervals and see how the final results get distributed [see Figs. 5(b) and 5(c)]. In this way one is able to account for the possible conjoined effects of the input parameters and produce fair estimates for the uncertainties in m_{spin} and m_{orb}.

From the sum-rule analysis, we obtain $m_{\text{spin}} = (2.0 \pm 0.3)\mu_B$/atom for V and $m_{\text{spin}} = (2.3 \pm 0.5)\mu_B$/atom for Cr. The orbital sum rule reveals an almost negligible value of $m_{\text{orb}} = (-0.01 \pm 0.02)\mu_B$/atom for Cr, while that of V is $m_{\text{orb}} = (-0.38 \pm 0.05)\mu_B$/atom. Thus, the small m_{orb} of the Cr ion does not significantly contribute to the total magnetic moment, suggesting a quenched Cr $3d$ orbital magnetic moment. The V ion carries a moderate orbital magnetic moment, indicating the partial quenching of m_{orb}. The antiparallel alignment of m_{spin} and m_{orb} agrees with Hund's last rule for less than half-filled shells. It is worth mentioning that due to the $2p$-$3d$ core hole correlation effects in $L_{2,3}$ absorption spectra and various approximations made deriving the sum rules, as well as the ambiguity in the choice of the integration range and the definition of the number of $3d$ holes, the moments calculated using sum rules can strongly deviate from their true values [61]. For this reason, we obtain more reliable spin and orbital magnetic moments by fitting theoretical spectra to the experimental ones, as will be discussed below.

C. MLFT analysis of the V and Cr spectra

In order to interpret our XAS and XMCD results and evaluate several physical parameters that control the electronic and magnetic properties of our V- and Cr-doped three-dimensional (3D) TIs, we have analyzed the experimental spectra using MLFT calculations. The calculated XAS/XMCD spectra, plotted as dashed-dotted lines in Figs. 3(a) and 3(b), fit well with the experimental data, reproducing all essential multiplet features of the measured spectra. A good agreement is most notable for the XMCD spectra (green dashed-dotted lines). Special attention was paid to reproduce all spectral features and their relative energy positions denoted by vertical dashed lines, especially the double-peak feature in the L_3 edge. The fact that a single realization of a local cluster is sufficient to reproduce the form of the experimental spectra rules out the coexistence of distinct impurity valencies on different sites, as well as the simultaneous incorporation in the van der Waals gap or metallic impurity segregation. Optimized values of the Slater integrals and spin-orbit coupling constants used in the calculations for the V $2p^6 3d^2$ and Cr $2p^6 3d^3$ initial states and for the V $2p^5 3d^3$ and Cr $2p^5 3d^4$ final states are shown in Table I. The listed Slater integrals indicate reductions to 65% (V) and 70% (Cr) of their original Hartree-Fock values. Due to the relaxation of atomic orbitals upon the $2p \rightarrow 3d$ excitation, we used separate sets of Slater integrals and the spin-orbit coupling constants ζ_{3d} for the initial and final states, which improves the agreement between the calculated and experimental spectra.

The parameters used for the calculations best reproducing our data are listed in Table II. It is well known that complex

TABLE II. Input parameters for the MLFT calculations obtained from the fit of XAS/XMCD spectra for $V_{0.1}Sb_{1.9}Te_3$ and $Cr_{0.1}(Bi_{0.1}Sb_{0.9})_{1.9}Te_3$ (in units of eV).

	$10Dq$	Δ	U_{dd}	U_{pd}	V_{e_g}	$V_{t_{2g}}$
$V_{0.1}Sb_{1.9}\,Te_3$	1.1	−2.5	3.8	4.6	1.1	0.65
$Cr_{0.1}\,(Bi_{0.1}Sb_{0.9})_{1.9}\,Te_3$	1.2	−2.0	3.5	4.2	1.4	0.82

TABLE III. Configuration contribution to the ground state [see Eq. (1)], electron occupation n_d, and z component of orbital and spin angular momenta in units of $\hbar$, for V- and Cr-doped samples. The relative errors do not exceed about 10% and were estimated by varying the fit parameters to obtain statistically significant deviations between the modeled and measured XAS/XMCD spectra.

Ion	Expectation value	d^2	d^3	d^4	d^5	d^6	total
V^{3+}	$\langle\Psi_n\|\Psi_n\rangle$	0.049	0.484	0.413	0.054		1.000
	$\langle\Psi_n\|\hat{n}_d\|\Psi_n\rangle$	0.098	1.452	1.652	0.270		3.472
	$\langle\Psi_n\|\hat{L}_z\|\Psi_n\rangle$	0.062	0.306	0.169	0.015		0.552
	$\langle\Psi_n\|\hat{S}_z\|\Psi_n\rangle$	−0.049	−0.565	−0.514	−0.065		−1.193
Cr^{3+}	$\langle\Psi_n\|\Psi_n\rangle$		0.104	0.500	0.354	0.042	1.000
	$\langle\Psi_n\|\hat{n}_d\|\Psi_n\rangle$		0.312	2.000	1.770	0.246	4.328
	$\langle\Psi_n\|\hat{L}_z\|\Psi_n\rangle$		0.007	0.019	0.004	0.000	0.030
	$\langle\Psi_n\|\hat{S}_z\|\Psi_n\rangle$		−0.156	−0.808	−0.586	−0.059	−1.609

nonlinear fits [62] may be weakly sensitive to some of the fit parameters [63]. In our particular case we were fitting simultaneously the XAS and XMCD spectra, which greatly mitigates these kinds of problems. For example, XAS is weakly sensitive to the CT energy Δ and the on-site Coulomb repulsion U_{dd}, but inclusion of the XMCD into the merit function restores the sensitivity to these parameters. Having pinned down the optimal fit parameters by minimizing the merit function, we then checked the robustness by varying the parameters around their optimal values in an uncorrelated manner, until a significant deviation between the modeled and measured data was obtained. In this way we were able to determine the uncertainties of the optimized fit values and the resulting d-shell occupation n_d, and of the orbital and spin moments (see Table III).

The experimental and theoretical values of the input parameters listed in Table II are well known for oxides [49,64,65]. For our compounds, in contrast to the oxides with more electronegative O ligands, one would expect a lower CT energy Δ, down to negative values as in the case of Cr_2Te_3 [54]. Prior to discussing our MLFT calculations, for simplicity, we can assume zero hoppings to the Te ligands. In this case, for the negative energy difference, $\Delta = E(d^{n+1}\underline{L}) - E(d^n)$, not the nominal configuration d^n, but the one with a ligand hole ($d^{n+1}\underline{L}$) becomes the actual ground state (see Fig. 2).

Indeed, the optimal fit yields $\Delta = -2.5$ eV for V and $\Delta = -2.0$ eV for Cr. As expected from the simplified considerations, these negative CT energies lead to a strong deviation from the nominal 3+ ionic ground state (see Table III). The effect of the negative CT energy is so profound that the contribution of the nominal configuration is less than ∼10%.

Furthermore, the nonvanishing hoppings used in the calculation result in a considerable contribution to the ground state from several different configurations, as illustrated in the inset to Fig. 3. The small weight of the last configuration indicates that three charge-transfer states along with the nominal configuration are already sufficient for a correct microscopic physical model.

The observed considerable contributions of different configurations might in part be due to the local contraction of the ligand atoms towards the TM ion, compared to the undisturbed Te-Sb distance. This contraction was demonstrated by *ab initio* calculations [27,66] and observed in extended x-ray absorption fine-structure (EXAFS) experiments [67], which show direct evidence of structural relaxations around TM ions.

The calculated total spin and orbital angular momenta, as well as d-shell electron occupations, are listed in Table III. The resulting number of $3d$ electrons is $n_d = 3.47$ for V and $n_d = 4.33$ for Cr, which is much larger than the nominal $n_d = 2$ for V^{3+} and $n_d = 3$ for Cr^{3+} ions. In this context, it is worth noting that our analysis is consistent with a picture in which the electronic charge is redistributed within the (V/Cr)-Te covalent bonds and does not contribute to the free carrier concentration.

For an isolated d shell with d^3, d^4, or d^5 filling, placed in a crystal field of octahedral symmetry, one would expect a *complete* quenching of the orbital angular momentum and corresponding magnetic moment [68]. In reality, the orbital angular momentum is always partially unquenched. Among the reasons for the unquenching one would name spin-orbit coupling and hybridization with ligands. Indeed, for Cr we find an almost completely quenched orbital magnetic moment $m_{\mathrm{orb}} = -0.03\mu_{\mathrm{B}}$, mainly determined by the contribution of the $d^4\underline{L}$ configuration to the ground state, as can be seen in Table III. In contrast, we see that both in experiment and theory vanadium consistently exhibits a much larger $m_{\mathrm{orb}} = -0.55\mu_{\mathrm{B}}$, determined by the contribution of the $d^3\underline{L}$ and $d^4\underline{L}^2$ configurations. In view of comparable spin-orbit couplings and hybridization with the ligands, this may first seem unexpected. However, even in the aforementioned simple model of quenching [68], the d-shell filling plays a decisive role. In our realistic case, due to the complex interplay between spin-orbit coupling, Coulomb repulsion, and hybridization to ligands, the resulting effect can only be understood quantitatively. To illustrate this in more detail, we vary the charge-transfer energy Δ, which affects the d-shell electron occupation, and plot in Fig. 6 the resulting expectation value of the orbital angular momentum. We clearly see how the increase of Δ leads to the expected decrease of d-shell occupation n_d and consequently to unquenching of the orbital moment. Hence, the difference between V and Cr becomes more evident, as the Cr has a larger d-shell filling.

Now, we can compare the magnetic moments obtained using the sum-rule analysis with those resulting from MLFT calculations. For V, the sum-rule-derived moments $m_{\mathrm{spin}} = (2.0 \pm 0.3)\mu_{\mathrm{B}}$/atom and $m_{\mathrm{orb}} = (-0.38 \pm 0.05)\mu_{\mathrm{B}}$/atom are reasonably close to the calculated $m_{\mathrm{spin}} = 2.39\mu_{\mathrm{B}}$/atom and

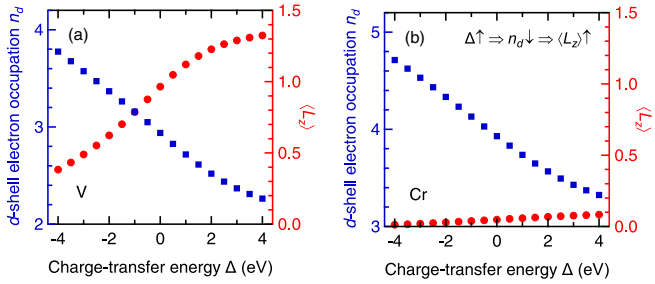

FIG. 6. d-shell electron occupation n_d (blue squares) and expectation value of the orbital angular momentum $\langle L_z \rangle$ (red circles) of (a) V and (b) Cr as functions of the charge-transfer energy Δ.

$m_{\mathrm{orb}} = -0.55\mu_{\mathrm{B}}$/atom. This considerable m_{orb} could be related to the substantial magnetocrystalline anisotropy experimentally observed in V-doped Sb_2Te_3 [7,12]. As for Cr, the sum rules provide a consistent value for the orbital magnetic moment $m_{\mathrm{orb}} = (-0.01 \pm 0.02)\mu_{\mathrm{B}}$/atom, but not for the spin magnetic moment. The sum-rule-derived spin moment for Cr $m_{\mathrm{spin}} = (2.3 \pm 0.5)\mu_{\mathrm{B}}$/atom is much smaller than the calculated one, $m_{\mathrm{spin}} = 3.22\mu_{\mathrm{B}}$, which could be attributed to the ambiguity in disentangling the overlapping Cr and Te edges. After all, the calculated total magnetic moments, $m_{\mathrm{tot}} = -2\langle S_z \rangle - \langle L_z \rangle = 1.84\mu_{\mathrm{B}}$/atom for V and $m_{\mathrm{tot}} = 3.19\mu_{\mathrm{B}}$/atom for Cr, are consistent with superconducting quantum interference device (SQUID) measurements [12] and recent density functional theory (DFT) calculations [27,33] for these systems.

D. Sb and Te $M_{4,5}$ XAS and XMCD

Our results confirm a strong charge-transfer effect from the host into the TM 3d states, with an enhanced covalency and a considerable pd hybridization taking place between TM dopants and the host material. The strong pd hybridization is an important indicator for determining the type of exchange-coupling mechanism and understanding ferromagnetism in these systems. It could induce magnetic moments at the otherwise nonmagnetic Te and Sb atoms in the host lattice. To confirm this, we have measured XMCD spectra at the Sb and Te $M_{4,5}$ absorption edges. Figures 7(a) and 7(b) show XAS spectra (top panels) and XMCD spectra (bottom panels) measured at the Sb $M_{4,5}$ edges of Cr- and V-doped samples, respectively. A clear reversal of left- and right-circularly polarized XAS intensities (blue and red curves, respectively) between the Sb M_5 and M_4 edges indicates a substantial dichroism at the Sb site. The atomic concentration of Cr and V is identical in the respective samples, hence we can directly compare the strength of Sb XMCD between Cr- and V-doped samples. To do so, we have normalized the signal to the area under the Sb M_4 edge after an accurate background correction. The M_4 edge was chosen due to the overlap of the Sb M_5 edge with the O K edge at 532 eV (the oxygen contamination comes from the beamline and shows no dichroism), which could lead to less reliable results. Moreover, for the V-doped sample the Sb M_5 absorption edge is close to the V L_2 edge, which leads to an overlap of XMCD signals as seen in the low-energy tail of the XMCD spectrum in the bottom panel of Fig. 7(b). Using a mean-square deviation from zero as a measure for the dichroic strength, we found Sb XMCD to be 20% stronger in the Cr-doped sample than in the V-doped one.

Figure 8 shows the circularly polarized XAS spectra of the V-doped sample measured at the Te $M_{4,5}$ edges in an external magnetic field of 3 T. The corresponding XMCD spectrum plotted in green reveals a small magnetic moment induced at the Te site. Due to the very small size of the Te XMCD signal, this becomes a very challenging measurement, especially for thin films, requiring a high signal quality and considerable

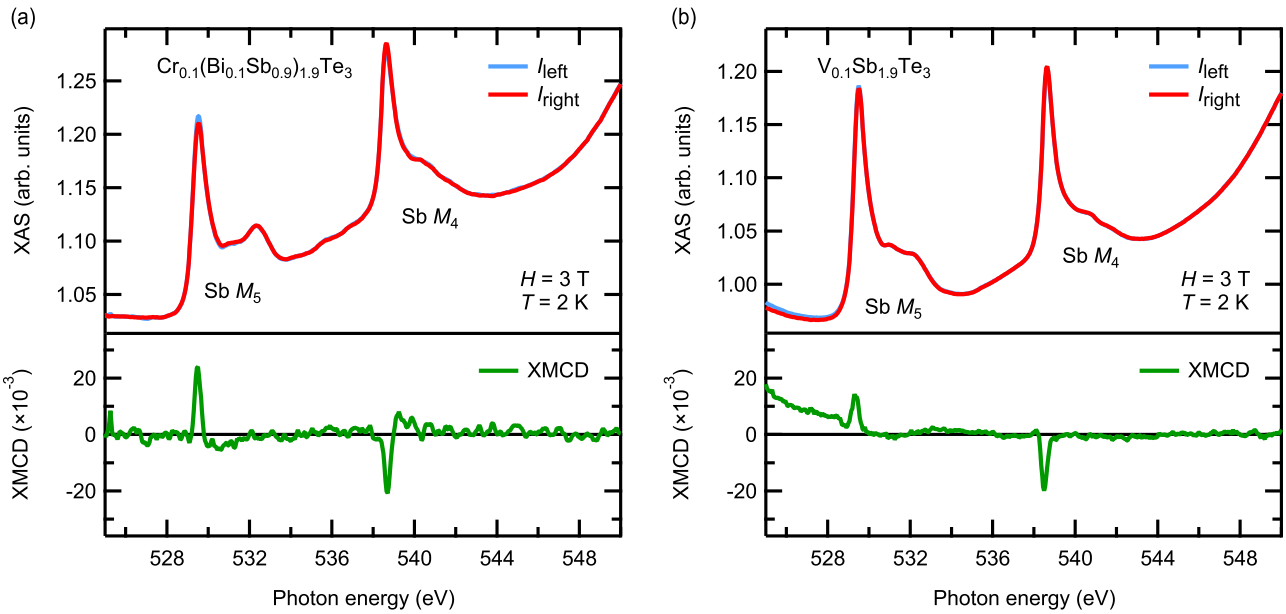

FIG. 7. XAS and XMCD spectra measured around the Sb $M_{4,5}$ edges ($3d \rightarrow 5p$) of (a) $Cr_{0.1}(Bi_{0.1}Sb_{0.9})_{1.9}Te_3$ and (b) $V_{0.1}Sb_{1.9}Te_3$. Top panel: XAS spectra for left- (light blue curve) and right- (dark red curve) circularly polarized x rays. Bottom panel: Normalized XMCD spectra (green curve).

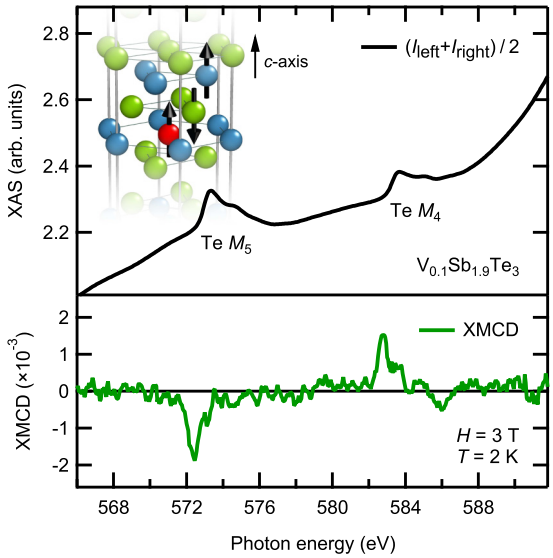

FIG. 8. Averaged XAS (black curve) measured at the Te $M_{4,5}$ edges ($3d \rightarrow 5p$) of $V_{0.1}Sb_{1.9}Te_3$ film. The green curve shows the corresponding XMCD spectrum ($I_{left} - I_{right}$) measured at $T = 2$ K and $H = 3$ T. The inset illustrates the relative magnetic moment orientations of the TM ion and neighboring Te and Sb atoms within the one quintuple layer.

statistics. Remarkably, here we were able to measure XMCD at the $M_{4,5}$ edges with a robust XMCD line shape showing a reversal of the XMCD sign between the M_4 and M_5 edges. As illustrated in Fig. 3(a), the spectra of the Cr-doped sample exhibit XMCD at the Te $M_{4,5}$ edges as well. However, the strong energy overlap of the Te $M_{4,5}$ and the Cr $L_{2,3}$ edges in this sample hinders the direct comparison of Te XMCD strength with the V-doped system.

In general, the strength of XMCD at the Sb and Te sites is expected to depend on the TM doping concentration and the degree of *pd* hybridization [25,33,53]. One might assume that Sb has a pure ionic configuration [Kr] $4d^{10}\,5s^2\,5p^0$ with complete shells, and hence should exhibit no induced moment. However, this is not fully correct. In the Sb_2Te_3 systems, similar to the diluted semiconductors [20,21], the p states are the main charge carriers. Thus the Sb $5p$ shell is not empty and exhibits a magnetic moment induced by the exchange interaction between the V/Cr and the Sb, even though it is of longer range than that between V/Cr and Te. So the same effect which results in a measurable XMCD at the Te $M_{4,5}$ edge also yields a nonvanishing XMCD at the Sb $M_{4,5}$ edge. This is further supported by the DFT analysis, showing that the main contribution to the magnetic moments of Sb and Te results from the p states [24,33,53].

Further, we notice that the similar intensity of the XMCD signal with opposite signs at the M_5 and M_4 edges suggests, according to the sum rules, that the total magnetic moments at the Sb/Te sites are dominated by the contribution of the spin magnetic moment. However, uncertainties in the background determination and in the separation of the spectral weight of the Sb M_5 edge from the weight of the V edges, which lie a few eV below, prohibit a quantitative statement. The sign of the XMCD signal allows us to derive the mutual orientation of the moments at the TM substituent and the neighboring Te and Sb atoms. Keeping in mind that the V/Cr $L_{2,3}$ edges correspond to a $2p \rightarrow 3d$ transition, whereas the Sb/Te $M_{4,5}$ edges correspond to a $3d \rightarrow 5p$ transition, the opposite sign of XMCD for the V/Cr and Sb edges indicates a parallel coupling between the V/Cr $3d$ and Sb $5p$ moments, and the same sign of V/Cr and Te XMCD indicates an antiparallel alignment of their moments [69]. Hence, the relative magnetic moment orientations can be summarized as (TM, Sb) ↑ -(Te) ↓ (see also the inset of Fig. 8), in good agreement with theoretical predictions [33].

V. SUMMARY

We have studied the electronic and magnetic properties of V- and Cr-doped thin films of the TI $(Bi, Sb)_2Te_3$. Similar to our earlier works [70,71], we have constructed a MLFT model for the TM dopants in $(Bi, Sb)_2Te_3$. By analyzing the experimental XAS and XMCD, we obtained the values for the charge-transfer, Coulomb repulsion, and hybridization energies, as well as for the crystal-field and Slater integrals, which will serve as an important input to future atomic multiplet calculations on similar systems.

The model clearly shows a strong charge transfer from the Te ligands to the V/Cr $3d$ states, such that the nominally ionic $3+$ configuration contributes less than 10% to the ground state, while the major contribution is due to configurations with one and two ligand holes. This observation can be understood as a combined effect of a strongly negative charge-transfer energy and a considerable hybridization between TM $3d$ and ligand $5p$ states. The *pd* hybridization and, hence the admixture of different configurations, might in part be due to the local relaxation of the ligands toward the TM, as evidenced by *ab initio* calculations [66] and EXAFS experiments [67].

The MLFT fits allowed us to circumvent the inadequacy of the XMCD spin sum rule for the early transition metals and determine the orbital and spin moments directly from the many-particle ground state. In good agreement with published magnetometry data [12,34], we have obtained total magnetic moments of $3.19\mu_B$ for Cr and $1.84\mu_B$ for V. In formal agreement with the expected quenching of the orbital moment for the d^3 configuration, the orbital magnetic moment on Cr is negligibly small, whereas for V we obtain $-0.55\mu_B$. The seeming violation of this expectation is a natural outcome of the d-shell filling, non-negligible hoppings to the ligands and effects of the spin-orbit interaction. The unquenched orbital moment could explain the substantial magnetocrystalline anisotropy observed in V-doped samples [7,12].

Our measurements further show that not only do the magnetic dopants V and Cr carry a magnetic moment, but also the nominally nonmagnetic host atoms Sb and Te possess spin-derived moments. The magnetism of the Sb and Te atoms suggests that the observed local magnetic coupling mechanism might be in part mediated by Sb/Te $5p$ states through *pd* hybridization, following the Zener-type *pd*-exchange interaction scenario [16,19,24,25,33]. Indeed, our work shows that *pd* hybridization yields a strong entanglement between charge transfer and magnetic ground state.

We provide a detailed microscopic insight into the electronic and magnetic properties of the magnetically doped 3D TI. Our results show that V with a d-shell electron occupation

of $n_d = 3.47$ exhibits a more robust FM order as compared to Cr with $n_d = 4.33$, confirming the spin-polarized first-principles calculations by Vergniory *et al.* [25], which showed that the effective exchange interaction is reduced with the number of d electrons per TM atom. The differences in the magnetic ground state between V and Cr imply differences in the 3d local density of states, as recently observed in scanning tunneling spectroscopy [72] and resPES [23]. This could point to the origin of the more robust realization of the ideal QAH state in V-doped systems as compared to Cr-doped systems. A deeper insight would require a systematic element-specific study of the ground-state electronic and magnetic properties of V and Cr impurities at the thresholds of the QAH effect and the recently reported metal-insulator transition at mK temperatures [73].

ACKNOWLEDGMENTS

This work was funded by the Deutsche Forschungsgemeinschaft (DFG, German Research Foundation) Project-ID 258499086–SFB 1170 (projects C04, C06, A01, and B01). We thankfully acknowledge Maurits W. Haverkort for fruitful discussions. R.J.G. was supported by the Natural Sciences and Engineering Research Council of Canada (NSERC). We acknowledge ALBA for beamtime provision under experimental Proposal No. 2017082310.

[1] M. Z. Hasan and C. L. Kane, Rev. Mod. Phys. **82**, 3045 (2010).
[2] X.-L. Qi and S.-C. Zhang, Rev. Mod. Phys. **83**, 1057 (2011).
[3] M. König, S. Wiedmann, C. Brüne, A. Roth, H. Buhmann, L. W. Molenkamp, X.-L. Qi, and S.-C. Zhang, Science **318**, 766 (2007).
[4] R. Yu, W. Zhang, H.-J. Zhang, S.-C. Zhang, X. Dai, and Z. Fang, Science **329**, 61 (2010).
[5] J. S. Dyck, W. Chen, P. Hájek, P. Lošt'ák, and C. Uher, Physica B **312-313**, 820 (2002).
[6] Z. Zhou, Y.-J. Chien, and C. Uher, Appl. Phys. Lett. **87**, 112503 (2005).
[7] J. S. Dyck, Č. Drašar, P. Lošt'ák, and C. Uher, Phys. Rev. B **71**, 115214 (2005).
[8] J. Choi, S. Choi, J. Choi, Y. Park, H.-M. Park, H.-W. Lee, B.-C. Woo, and S. Cho, Phys. Status Solidi B **241**, 1541 (2004).
[9] Y. S. Hor, P. Roushan, H. Beidenkopf, J. Seo, D. Qu, J. G. Checkelsky, L. A. Wray, D. Hsieh, Y. Xia, S.-Y. Xu, D. Qian, M. Z. Hasan, N. P. Ong, A. Yazdani, and R. J. Cava, Phys. Rev. B **81**, 195203 (2010).
[10] V. Kulbachinskii, A. Kaminskii, K. Kindo, Y. Narumi, K. Suga, P. Lostak, and P. Svanda, Physica B **311**, 292 (2002).
[11] C.-Z. Chang, J. Zhang, X. Feng, J. Shen, Z. Zhang, M. Guo, K. Li, Y. Ou, P. Wei, L.-L. Wang, Z.-Q. Ji, Y. Feng, S. Ji, X. Chen, J. Jia, X. Dai, Z. Fang, S.-C. Zhang, K. He, Y. Wang, L. Lu, X.-C. Ma, and Q.-K. Xue, Science **340**, 167 (2013).
[12] C.-Z. Chang, W. Zhao, D. Y. Kim, H. Zhang, B. A. Assaf, D. Heiman, S.-C. Zhang, C. Liu, M. H. W. Chan, and J. S. Moodera, Nat. Mater. **14**, 473 (2015).
[13] S. Grauer, S. Schreyeck, M. Winnerlein, K. Brunner, C. Gould, and L. W. Molenkamp, Phys. Rev. B **92**, 201304(R) (2015).
[14] J. G. Checkelsky, R. Yoshimi, A. Tsukazaki, K. S. Takahashi, Y. Kozuka, J. Falson, M. Kawasaki, and Y. Tokura, Nat. Phys. **10**, 731 (2014).
[15] K. He, Y. Wang, and Q.-K. Xue, Nat. Sci. Rev. **1**, 38 (2013).
[16] J. Kim, S.-H. Jhi, A. H. MacDonald, and R. Wu, Phys. Rev. B **96**, 140410(R) (2017).
[17] C.-Z. Chang, J. Zhang, M. Liu, Z. Zhang, X. Feng, K. Li, L.-L. Wang, X. Chen, X. Dai, Z. Fang, X.-L. Qi, S.-C. Zhang, Y. Wang, K. He, X.-C. Ma, and Q.-K. Xue, Adv. Mater. **25**, 1065 (2013).
[18] X. Kou, M. Lang, Y. Fan, Y. Jiang, T. Nie, J. Zhang, W. Jiang, Y. Wang, Y. Yao, L. He, and K. L. Wang, ACS Nano **7**, 9205 (2013).
[19] J. Kim, H. Wang, and R. Wu, Phys. Rev. B **97**, 125118 (2018).
[20] K. Sato, L. Bergqvist, J. Kudrnovský, P. H. Dederichs, O. Eriksson, I. Turek, B. Sanyal, G. Bouzerar, H. Katayama-Yoshida, V. A. Dinh, T. Fukushima, H. Kizaki, and R. Zeller, Rev. Mod. Phys. **82**, 1633 (2010).
[21] D. J. Keavney, D. Wu, J. W. Freeland, E. Johnston-Halperin, D. D. Awschalom, and J. Shi, Phys. Rev. Lett. **91**, 187203 (2003).
[22] M. Li, C.-Z. Chang, L. Wu, J. Tao, W. Zhao, M. H. W. Chan, J. S. Moodera, J. Li, and Y. Zhu, Phys. Rev. Lett. **114**, 146802 (2015).
[23] T. R. F. Peixoto, H. Bentmann, S. Schreyeck, M. Winnerlein, C. Seibel, H. Maaß, M. Al-Baidhani, K. Treiber, S. Schatz, S. Grauer, C. Gould, K. Brunner, A. Ernst, L. W. Molenkamp, and F. Reinert, Phys. Rev. B **94**, 195140 (2016).
[24] M. Ye, T. Xu, G. Li, S. Qiao, Y. Takeda, Y. Saitoh, S.-Y. Zhu, M. Nurmamat, K. Sumida, Y. Ishida, S. Shin, and A. Kimura, Phys. Rev. B **99**, 144413 (2019).
[25] M. G. Vergniory, M. M. Otrokov, D. Thonig, M. Hoffmann, I. V. Maznichenko, M. Geilhufe, X. Zubizarreta, S. Ostanin, A. Marmodoro, J. Henk, W. Hergert, I. Mertig, E. V. Chulkov, and A. Ernst, Phys. Rev. B **89**, 165202 (2014).
[26] J.-M. Zhang, W. Zhu, Y. Zhang, D. Xiao, and Y. Yao, Phys. Rev. Lett. **109**, 266405 (2012).
[27] J.-M. Zhang, W. Ming, Z. Huang, G.-B. Liu, X. Kou, Y. Fan, K. L. Wang, and Y. Yao, Phys. Rev. B **88**, 235131 (2013).
[28] X. F. Kou, W. J. Jiang, M. R. Lang, F. X. Xiu, L. He, Y. Wang, Y. Wang, X. X. Yu, A. V. Fedorov, P. Zhang, and K. L. Wang, J. Appl. Phys. **112**, 063912 (2012).
[29] J. Stöhr, J. Electron. Spectrosc. Relat. Phenom. **75**, 253 (1995).
[30] G. van der Laan and B. T. Thole, Phys. Rev. B **43**, 13401 (1991).
[31] A. I. Figueroa, G. van der Laan, L. J. Collins-McIntyre, S.-L. Zhang, A. A. Baker, S. E. Harrison, P. Schönherr, G. Cibin, and T. Hesjedal, Phys. Rev. B **90**, 134402 (2014).
[32] L. B. Duffy, A. I. Figueroa, L. Gładczuk, N.-J. Steinke, K. Kummer, G. van der Laan, and T. Hesjedal, Phys. Rev. B **95**, 224422 (2017).
[33] M. F. Islam, C. M. Canali, A. Pertsova, A. Balatsky, S. K. Mahatha, C. Carbone, A. Barla, K. A. Kokh, O. E. Tereshchenko, E. Jiménez, N. B. Brookes, P. Gargiani,

M. Valvidares, S. Schatz, T. R. F. Peixoto, H. Bentmann, F. Reinert, J. Jung, T. Bathon, K. Fauth, M. Bode, and P. Sessi, Phys. Rev. B **97**, 155429 (2018).
[34] L. B. Duffy, A. I. Figueroa, G. van der Laan, and T. Hesjedal, Phys. Rev. Mater. **1**, 064409 (2017).
[35] P. Sessi, R. R. Biswas, T. Bathon, O. Storz, S. Wilfert, A. Barla, K. A. Kokh, O. E. Tereshchenko, K. Fauth, M. Bode, and A. V. Balatsky, Nat. Commun. **7**, 12027 (2016).
[36] J. A. Krieger, C.-Z. Chang, M.-A. Husanu, D. Sostina, A. Ernst, M. M. Otrokov, T. Prokscha, T. Schmitt, A. Suter, M. G. Vergniory, E. V. Chulkov, J. S. Moodera, V. N. Strocov, and Z. Salman, Phys. Rev. B **96**, 184402 (2017).
[37] M. Winnerlein, S. Schreyeck, S. Grauer, S. Rosenberger, K. M. Fijalkowski, C. Gould, K. Brunner, and L. W. Molenkamp, Phys. Rev. Mater. **1**, 011201(R) (2017).
[38] N. V. Tarakina, S. Schreyeck, M. Duchamp, G. Karczewski, C. Gould, K. Brunner, R. E. Dunin-Borkowski, and L. W. Molenkamp, CrystEngComm **19**, 3633 (2017).
[39] A. Barla, J. Nicolás, D. Cocco, S. M. Valvidares, J. Herrero-Martín, P. Gargiani, J. Moldes, C. Ruget, E. Pellegrin, and S. Ferrer, J. Synchrotron Radiat. **23**, 1507 (2016).
[40] C. I. Fornari, P. H. O. Rappl, S. L. Morelhão, T. R. F. Peixoto, H. Bentmann, F. Reinert, and E. Abramof, APL Mater. **4**, 106107 (2016).
[41] F. de Groot and A. Kotani, *Core Level Spectroscopy of Solids*, Advances in Condensed Matter Science Vol. 6 (Taylor & Francis, London, 2008).
[42] B. T. Thole, G. van der Laan, J. C. Fuggle, G. A. Sawatzky, R. C. Karnatak, and J.-M. Esteva, Phys. Rev. B **32**, 5107 (1985).
[43] J. P. Crocombette and F. Jollet, J. Phys.: Condens. Matter **8**, 5253 (1996).
[44] R. Zimmermann, P. Steiner, R. Claessen, F. Reinert, S. Hüfner, P. Blaha, and P. Dufek, J. Phys.: Condens. Matter **11**, 1657 (1999).
[45] W. Liu, Y. Xu, L. He, G. van der Laan, R. Zhang, and K. Wang, Sci. Adv. **5**, eaav2088 (2019).
[46] B. Leedahl, D. W. Boukhvalov, E. Z. Kurmaev, A. Kukharenko, I. S. Zhidkov, N. V. Gavrilov, S. O. Cholakh, P. H. Le, C. W. Luo, and A. Moewes, Sci. Rep. **7**, 5758 (2017).
[47] P. Mahadevan and D. D. Sarma, Phys. Rev. B **61**, 7402 (2000).
[48] A. E. Bocquet, A. Fujimori, T. Mizokawa, T. Saitoh, H. Namatame, S. Suga, N. Kimizuka, Y. Takeda, and M. Takano, Phys. Rev. B **45**, 1561 (1992).
[49] A. E. Bocquet, T. Mizokawa, T. Saitoh, H. Namatame, and A. Fujimori, Phys. Rev. B **46**, 3771 (1992).
[50] O. K. Andersen, W. Klose, and H. Nohl, Phys. Rev. B **17**, 1209 (1978).
[51] A. Fujimori and F. Minami, Phys. Rev. B **30**, 957 (1984).
[52] M. W. Haverkort, M. Zwierzycki, and O. K. Andersen, Phys. Rev. B **85**, 165113 (2012).
[53] M. Ye, W. Li, S. Zhu, Y. Takeda, Y. Saitoh, J. Wang, H. Pan, M. Nurmamat, K. Sumida, F. Ji, Z. Liu, H. Yang, Z. Liu, D. Shen, A. Kimura, S. Qiao, and X. Xie, Nat. Commun. **6**, 8913 (2015).
[54] K. Yaji, A. Kimura, C. Hirai, M. Taniguchi, M. Koyama, H. Sato, K. Shimada, A. Tanaka, T. Muro, S. Imada, and S. Suga, Phys. Rev. B **70**, 064402 (2004).
[55] C. T. Chen, Y. U. Idzerda, H.-J. Lin, N. V. Smith, G. Meigs, E. Chaban, G. H. Ho, E. Pellegrin, and F. Sette, Phys. Rev. Lett. **75**, 152 (1995).
[56] B. T. Thole, P. Carra, F. Sette, and G. van der Laan, Phys. Rev. Lett. **68**, 1943 (1992).
[57] P. Carra, B. T. Thole, M. Altarelli, and X. Wang, Phys. Rev. Lett. **70**, 694 (1993).
[58] M. W. Haverkort, Spin and orbital degrees of freedom in transition metal oxides and oxide thin films studied by soft x-ray absorption spectroscopy, Ph.D. thesis, Universität zu Köln, 2005.
[59] K. W. Edmonds, N. R. S. Farley, T. K. Johal, G. van der Laan, R. P. Campion, B. L. Gallagher, and C. T. Foxon, Phys. Rev. B **71**, 064418 (2005).
[60] C. Piamonteze, P. Miedema, and F. M. F. de Groot, J. Phys.: Conf. Ser. **190**, 012015 (2009).
[61] A. Scherz, H. Wende, C. Sorg, K. Baberschke, J. Minár, D. Benea, and H. Ebert, Phys. Scr., T **115**, 586 (2005).
[62] R. Storn and K. Price, J. Global Optim. **11**, 341 (1997).
[63] J. Tiilikainen, V. Bosund, M. Mattila, T. Hakkarainen, J. Sormunen, and H. Lipsanen, J. Phys. D: Appl. Phys. **40**, 4259 (2007).
[64] A. E. Bocquet, T. Mizokawa, K. Morikawa, A. Fujimori, S. R. Barman, K. Maiti, D. D. Sarma, Y. Tokura, and M. Onoda, Phys. Rev. B **53**, 1161 (1996).
[65] A. Tanaka and T. Jo, J. Phys. Soc. Jpn. **63**, 2788 (1994).
[66] P. Larson and W. R. L. Lambrecht, Phys. Rev. B **78**, 195207 (2008).
[67] Z. Liu, X. Wei, J. Wang, H. Pan, F. Ji, F. Xi, J. Zhang, T. Hu, S. Zhang, Z. Jiang, W. Wen, Y. Huang, M. Ye, Z. Yang, and S. Qiao, Phys. Rev. B **90**, 094107 (2014).
[68] P. Fazekas, *Lecture Notes on Electron Correlation and Magnetism*, Series in Modern Condensed Matter Physics Vol. 5 (World Scientific, Singapore, 1999).
[69] A. Kimura, S. Suga, T. Shishidou, S. Imada, T. Muro, S. Y. Park, T. Miyahara, T. Kaneko, and T. Kanomata, Phys. Rev. B **56**, 6021 (1997).
[70] V. B. Zabolotnyy, K. Fürsich, R. J. Green, P. Lutz, K. Treiber, C.-H. Min, A. V. Dukhnenko, N. Y. Shitsevalova, V. B. Filipov, B. Y. Kang, B. K. Cho, R. Sutarto, F. He, F. Reinert, D. S. Inosov, and V. Hinkov, Phys. Rev. B **97**, 205416 (2018).
[71] K. Fürsich, V. B. Zabolotnyy, E. Schierle, L. Dudy, O. Kirilmaz, M. Sing, R. Claessen, R. J. Green, M. W. Haverkort, and V. Hinkov, Phys. Rev. B **97**, 165126 (2018).
[72] W. Zhang, D. West, S. H. Lee, Y. Qiu, C.-Z. Chang, J. S. Moodera, Y. S. Hor, S. Zhang, and W. Wu, Phys. Rev. B **98**, 115165 (2018).
[73] X. Kou, L. Pan, J. Wang, Y. Fan, E. S. Choi, W.-L. Lee, T. Nie, K. Murata, Q. Shao, S.-C. Zhang, and K. L. Wang, Nat. Commun. **6**, 8474 (2015).